

Observation of Plasma Bubble Structures in a GeV Laser-Plasma Accelerator

Yen-Yu Chang,¹ Kathleen Weichman,¹ Xiantao Cheng,¹ Joseph M. Shaw,¹ James Welch,¹ Maxwell LaBerge,¹ Andrea Hannasch,¹ Rafal Zgadzaj,¹ Aaron Bernstein,¹ Watson Henderson,¹ and Michael C. Downer^{1, a)}
Department of Physics, The University of Texas at Austin, Austin, Texas 78712-1081, USA

(Dated: 14 December 2024)

We measure characteristics of plasma bubbles in GeV-class laser-plasma accelerators (LPAs) using Faraday rotation diagnostics. We extend these techniques, previously demonstrated for LPAs in atmospheric density plasmas (electron density $n_e > 10^{19} \text{ cm}^{-3}$), to LPAs in low-density plasmas ($n_e \approx 5 \times 10^{17} \text{ cm}^{-3}$), in which plasma bubbles are ~ 5 times larger, and correspondingly easier to visualize in detail. The signals show $\approx 0.5^\circ$ rotation streaks of opposite sign separated by $\sim 50 \mu\text{m}$, consistent with bubble diameter; no on-axis rotation; streaks length consistent with transverse probe pulse duration ($180 \mu\text{m}$ for 500 fs pulse length, and $600 \mu\text{m}$ for 2 ps pulse length). We utilized an anamorphic imaging system to obtain a wide longitudinal field of view ($> 1 \text{ cm}$) and a high transverse resolution ($< 9 \mu\text{m}$). We also demonstrated that Faraday rotation signals are sensitive to the stages of acceleration processes using extended 2D Finite Difference Time Domain (FDTD) simulation.

I. INTRODUCTION

Since laser-plasma accelerators (LPAs) were first proposed in 1979¹, LPAs have become a tabletop source of quasi-monoenergetic GeV electron bunches² and ultrafast X-ray pulses³, for use in applications in biology, medicine, and materials science. The key to the compact size of LPAs is the unprecedented accelerating field (GeV/cm), contained in a light-speed, microscopic ($\sim 10^{-5} \text{ m}$) plasma structure, in comparison to the conventional metal cavity ($\sim 1 \text{ m}$) radio-frequency accelerators. In particular, the highest-performing LPAs operate in a strongly nonlinear "bubble" or "blow-out" regime⁴, where the driving laser pulse is intense enough to blow out electrons to form a plasma bubble.

Measuring the characteristics (e.g. size, shape, and bubble wall thickness) of plasma bubbles is essential to understanding the acceleration process of LPAs. The bubble structures^{5,6,4,7,8} and the self-injection threshold have been studied analytically^{7,9}, numerically¹⁰, and experimentally^{11,12}. In addition, Kalmykov *et al.*¹³ has suggested that the expansion rate of the plasma bubble has to exceed certain values to induce self-injection. Simulation¹⁴ has also suggested that in GeV-class LPAs, the plasma bubbles can experience two stages in the acceleration process. In the first stage, when the driving pulse enters the plasma, the intensity of the pulse oscillates until the spot size matches the self-guiding conditions. During the intensity oscillations, the bubble expands when the driving pulse intensity decreases (due to defocusing), which leads to periodic self-injection¹³. In the second stage, the bubble structures stabilizes and the driving pulse starts to experience temporal compression¹⁵ and etching effects¹⁶. The self-injection stops when the bubble stops expanding. The bubble

structures and bubble dynamics of GeV-class LPAs, however, have not been experimentally characterized due to low plasma density ($\sim 5 \times 10^{17} \text{ cm}^{-3}$) and long laser plasma interaction length ($\sim 10 \text{ cm}$).

Several previous experiments have visualized plasma bubble structures and dynamics in high density ($n_e \leq 10^{19} \text{ cm}^{-3}$) plasmas. Dong *et al.*¹⁷ showed that the bubble reshaped co-propagating chirped probe pulses into optical bullets, which in a single shot revealed bubble formation even below the threshold for relativistic electron production. However, Dong *et al.* did not observe dynamics or the internal structure of plasma bubbles. Li *et al.*¹⁸ observed dynamics of bubble formation, propagation and lengthening in a single shot by analyzing phase streaks imprinted on a chirped pulse propagating at a small angle to the bubble. Nevertheless, the thin bubble wall was not resolvable due to the limited probe bandwidth. Sávert *et al.*¹⁹ obtained shadowgraphic snapshots of bubbles using a transverse probe with pulse length $\leq 10 \text{ fs}$, and observed changes in bubble structure over multiple shots. As for GeV-class LPAs operating in low density plasmas ($n_e = 5 \times 10^{17} \text{ cm}^{-3}$), Li *et al.* have used Multi-object-plane technique to reveal the plasma bubble evolution in $\sim 3 \text{ cm}$ in single-shot²⁰. However, the complex phase shift induced by the plasma channel around the bubble made extracting the signal extremely challenging.

In addition, several investigators imaged Faraday rotation of a transverse probe pulse to measure the magnetic field inside²¹ and outside²² of the plasma bubbles, and to estimate the length of the accelerated electron bunch²³. In all of these previous studies, however, the plasma density n_e exceeded 10^{19} cm^{-3} , limiting bubble size to $\lambda_p \leq 10 \mu\text{m}$ and maximum accelerated electron energy to $\sim 100 \text{ MeV}$ due to dephasing and pump depletion limits. Moreover, the field of view of bubble propagation was limited to $\sim 3 \text{ mm}$.

In our experiments, we extended Faraday rotation diagnostics for the first time to plasma density in the range $2 < n_e < 5 \times 10^{17} \text{ cm}^{-3}$ — more than 20 times lower

^{a)}downer@physics.utexas.edu

than in previous work — for which bubble size is of order $\lambda_p \sim 50 \mu\text{m}$, and electron acceleration to multiple GeV is possible¹⁴. The rotation angle can be estimated by using

$$\phi_{\text{rot}} = \frac{e^3}{2c\epsilon_0 m_e^2 \omega^2} \int_{\ell} n_e \mathbf{B}_{\varphi} \cdot d\mathbf{s}, \quad (1)$$

where ω is the frequency of the probe beam, ℓ is the trajectory of the object, n_e is the plasma density, \mathbf{B}_{φ} is the azimuthal magnetic field, and $d\mathbf{s}$ is the path element along the path of the probe beam. Since n_e is almost zero inside the plasma bubble, ϕ_{rot} induced preferentially around the dense plasma bubble walls, on which the azimuthal magnetic induced by the accelerated electrons in relativistic regime scales as $\mathbf{B}_{\varphi} \propto N_{\text{tot}} \cdot \gamma / R_b^2 \propto N_{\text{tot}} \cdot E_{\text{electron}} \cdot n_e$, where N_{tot} is the total number of the accelerated electrons, γ is the Lorentz factor of the accelerated electrons, E_{electron} is the energy of the accelerated electrons, and $R_b \propto \lambda_p \propto n_e^{-1/2}$ is the bubble radius. Therefore, from the expression of the rotation angle, we have $\phi_{\text{rot}} \propto N_{\text{tot}} \cdot E_{\text{electron}} \cdot n_e^{3/2}$. Although n_e in our experiment was ~ 50 times lower than that in the previous experiments, N_{tot} and E_{electron} were around 10 and 40 times greater in our case. Eventually, the magnitude of the Faraday rotation angle in our experiment was around the same order of magnitude of the previous works.

Furthermore, we demonstrated that Faraday rotation signals are sensitive to transitions in the acceleration stages. Simulation⁷ and analytical models⁸ have previously suggested that the distribution of the dense plasma sheath around the bubble varies during the acceleration process. In the first stage of the acceleration where the driving pulse is self-focusing and the plasma bubble is expanding, the sheath electrons around the bubble experience long slippage time²⁴, gain the most energy, and therefore, are more likely to accumulate (to be trapped) on the back of the bubble²⁵. Hence the plasma density on the back of the bubble is high in the first stage, and the return current of the plasma sheath can also induce strong azimuthal magnetic field on the back of the bubble²⁵. In the second stage of the acceleration where the bubble stabilizes, the sheath electrons become less energetic and the population of the electrons on the back of the bubble is lower.

In this paper, we will show that Faraday rotation signals have different characteristics in different stages of the acceleration process using extended 2D (2D+1) Finite Difference Time Domain (FDTD) simulations. In the first stage, since the plasma density and magnetic field are both high on the back of the bubble, the Faraday rotation signal has large vertical width. In the second stage, the plasma density of the back of the bubble decreases, but the density on the thin side sheath remains high. Thus, the Faraday rotation signal has narrower vertical width and peaks at R_b (bubble radius)¹⁶ above the center line. Our experimental data indicate that the

transition from first stage to second stage occurs at 61% of full laser-plasma interaction length.

In section II of this paper, we will present the experimental setup. In section III, we show the experimental results. In section IV, we demonstrate the relation between the Faraday rotation signals and the plasma bubble structures using FDTD simulations.

II. EXPERIMENTAL PROCEDURE

Fig. 1 shows the schematic of the setup for measuring plasma bubble structures using Faraday rotation diagnostics at the Texas Petawatt Laser at the University of Texas at Austin.

A pump pulse with peak power 0.67 PW (100 J, 150 fs FWHM) at center wavelength $1.057 \mu\text{m}$ was focused at f/45 into a 1.5 mm radius entrance aperture of a 7 cm long gas cell filled with 5 Torr helium (He) with purity of 99.99%. The intense pump beam ionized the gas to generate plasmas ($n_{e0} \sim 2 \times 10^{17} \text{ cm}^{-3}$), self-focused, generated nonlinear plasma waves (plasma bubbles), and accelerated electrons to high energy. A synchronized probe pulse, split from the pump beam, propagated transversely through the side windows of the gas cell and overlapped with the plasma bubbles. The probe beam was linearly polarized with polarization parallel to that of the pump beam on target. The diameter of the probe beam was 2 cm, and the center of the probe beam was 3.8 cm away from the entrance aperture of the gas cell. In the first attempt, we chipped the pulse length of the probe pulse to 2 ps, and in the second attempt, the pulse length of the probe pulse was compressed to 500 fs.

One challenge of applying Faraday rotation diagnostics to GeV LPAs was acquiring a wide horizontal field of view while maintaining a reasonable vertical resolution. According to PIC simulations, the plasma bubbles can propagate multiple centimeters, and the transverse diameter of the bubbles, which is critical to Faraday rotation signals, ranges from $40 \mu\text{m}$ to $60 \mu\text{m}$. We used an anamorphic imaging system to demagnify the horizontal dimension to obtain wide field of view, but at the same time, magnify the vertical dimension to achieve a reasonable resolution.

The anamorphic imaging system consisted of three lenses (see Fig. 1(d)). Lens 1 was an objective lens with 15 cm focal length and 2" aperture to collect the light. Lens 2 was an 1" achromatic cylindrical lens with 25 cm focal length, and Lens 3 was an achromatic cylindrical lens with 5 cm focal length. The horizontal field of view of the imaging system was $\sim 1.1 \text{ cm}$ with $\sim 50 \mu\text{m}$ resolution, and the vertical field of view was $\sim 2.5 \text{ mm}$ with $\sim 8.8 \mu\text{m}$ resolution (see Fig. 2). The vertical resolution was determined by averaging the distances between the horizontal lines of the elements on the image of a USAF target, and $8.77 \mu\text{m}$ (group 5 element 6) was the smallest distance that could be resolved on the image. The depth of field was up to $300 \mu\text{m}$ (Fig. 2 (c)).

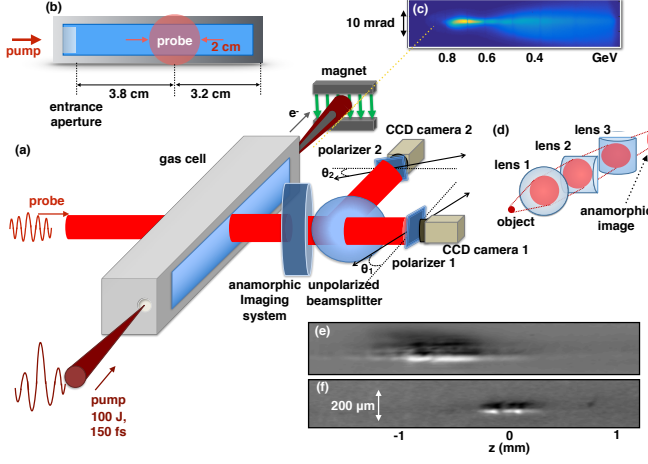


FIG. 1. The schematic of the GeV LPA and the Faraday rotation diagnostics along with the signals from one particular shot. (a) The layout of the setup. (b) The side view of the gas cell. (c) The electron spectrum. (d) The layout of the anamorphic imaging system. Lens 1 is a spherical achromatic doublet with $f_1 = 15$ cm. Lens 2 are both cylindrical achromatic doublets with $f_2 = 25$ cm and $f_3 = 5$ cm. (e) and (f) The Faraday rotation angles of two consecutive shots with pump-probe delay changed ~ 1.2 ps.

To acquire a high signal-to-noise ratio in the rotation angle measurement, we split the probe beam with an unpolarized beamsplitter after the imaging system and sent the split beams to two cameras with polarizers in front of them as has been done by other researchers^{21,23}. The two polarizers in front of the cameras were rotated away from extinction in opposite directions with a small angle approximately equal to the expected rotation angle values ($\theta_i = \pm 2^\circ$, $i = 1, 2$). Since the two polarizers rotated with biased angles, the regions where the Faraday rotation occurred and the polarization was rotated clockwise was brighter on one camera and dimmer on the other. The same was true of the counterclockwise rotation. The measured intensity $I_{pol,i}(y, z)$ can be described by Malus' law as

$$I_{pol,i}(y, z) = I_0(y, z) \cdot T_i \cdot (1 - \beta_i \cdot \cos^2(\phi_{rot}(y, z) - \theta_i))$$

where $I_0(y, z)$ is the intensity of the original probe beam, T_i is the transmission/reflection ratio of the beam splitter. β_i ($i = 1, 2$) is the extinction ratio of the polarizers, where $(1 - \beta_1) = 6.1 \times 10^{-3}$ and $(1 - \beta_2) = 3.1 \times 10^{-3}$. The rotation angle can be extracted by dividing the intensity of the two images $I_{pol,1}/I_{pol,2}$. We matched the images of the two cameras according to the calibrated reference point.

III. EXPERIMENTAL RESULTS

The Faraday rotation signals from the experiment are shown in Fig. 3 and Fig. 4, where the pump beam and the accelerated electrons propagate from left to right. Note that the vertical and horizontal axes in the plots are not to scale because the probe beam was imaged through an anamorphic imaging system. The Faraday rotation signals were observed only in conjunction with accelerated electrons. Since the low plasma density results in the absence of plasma shadowing on the images, we were unable to precisely locate the relative position of the pump beam and the rotation angle signal. Therefore, we did several preliminary shots until we saw a definite Faraday rotation signal (Fig. 1(e)), and then we delayed the probe beam ~ 1.2 ps (~ 0.4 mm) in subsequent shots, and the signal shifted correspondingly (Fig. 1(f)). This iterative process for shifting the probe beam showed that the rotation angle signals were indeed sensitive to the overlapping of the pump and the probe beams.

The region where the Faraday effect is the strongest is symmetric around the laser axis (Fig. 3(c)). Since the Faraday effect is induced by the coupling of the magnetic field and plasma density, the magnitude of the rotation angle should be at its maximum around the region of the dense plasma around the bubble walls. Hence the distance between the peaks and valleys indicates the transverse size of the plasma bubble. The vertical lineout of the rotation angle signal agrees reasonably with the FDTD simulation (Fig. 3(d)), which shows that the

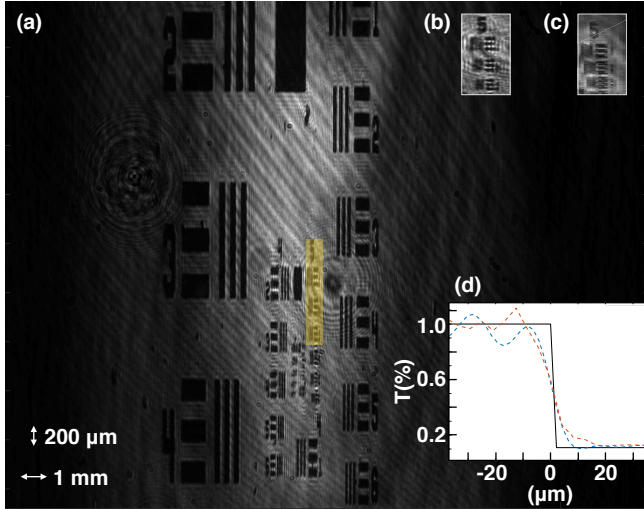


FIG. 2. The images of a USAF resolution target through the anamorphic imaging system. (a): The full image. (b): zoom in of in-focused image. (c): zoom in of the image that is $300 \mu\text{m}$ away from the in-focused image plane. (d) The averaged vertical lineout of group 4 element 2. Black solid line is the object. The blue dash line is the lineout when the image is in focus, and the red dash line is the lineout when the image is $300 \mu\text{m}$ out of focus. The vertical axis is the normalized transmission in percentage.

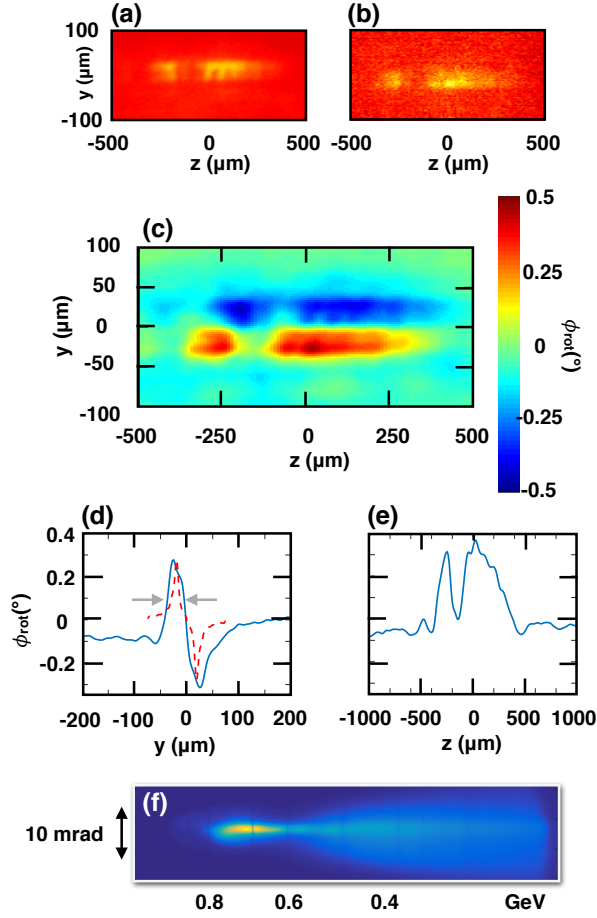


FIG. 3. The Faraday rotation signals with long probe pulse (2 ps). The z location of the signal is 4.08 cm away from the entrance aperture. (a) and (b) Raw images of camera 1 and 2. (c) The Faraday rotation signal converted from the raw images. (d) Blue line is the vertical lineout of the Faraday rotation signal averaged from $z = -230 \mu\text{m}$ to $250 \mu\text{m}$, and red dash line is the result of the FDTD simulation. (see Fig. 8) The FWHM of the peak is $35 \mu\text{m}$. (e) The horizontal lineout of the Faraday rotation signal averaged from $y = -40 \mu\text{m}$ to $0 \mu\text{m}$. (f) The energy spectrum of the electron on the same shot. The total charge above 300 MeV is 36.6 pC.

Faraday rotation happened dominantly around the bubble walls. The average transverse distance between the peaks and the valleys of the rotation angle is $\simeq 50.8 \pm 10.1 \mu\text{m}$, which matches the diameter of the plasma bubble ($R_p = \sqrt{a_0}/k_p \simeq 28.2 \mu\text{m}$, where R_p is the radius of the plasma bubble, $a_0 \simeq 3.5$ is the normalized vector potential², and $k_p = 0.13 \mu\text{m}^{-1}$).

The Faraday rotation signal indicated that the plasma bubble was fully blown out, and the horizontal length of the signal reflects the pulse length of the probe pulse. In Fig. 3(e) where the pulse length of the probe was 2 ps, the FWHM of the signal was $570 \mu\text{m}$, and in Fig. 4 (e) where the pulse length of the probe was 500 fs, the

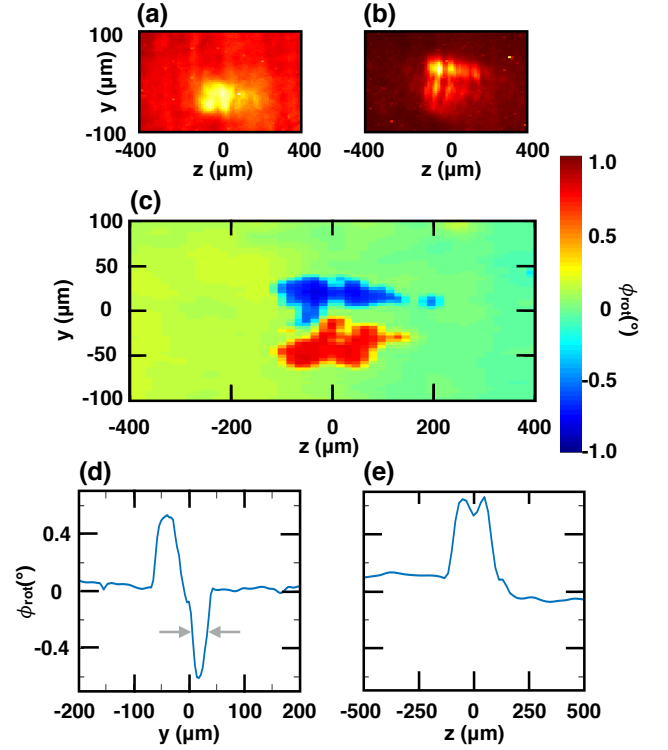


FIG. 4. The Faraday rotation signals with short probe pulse (500 fs). The z location of the signal is 4.263 cm away from the entrance aperture. (a) and (b) Raw images of camera 1 and 2. (c) The Faraday rotation signal converted from the raw images. (d) Blue line is the vertical lineout of the Faraday rotation signal averaged from $z = -120$ to $150 \mu\text{m}$. The FWHM of the valley is $25.1 \mu\text{m}$. (e) The horizontal lineout of the Faraday rotation signal averaged from $y = -70 \mu\text{m}$ to $-20 \mu\text{m}$.

FWHM of the signal was $180 \mu\text{m}$. Moreover, the vertical width of the Faraday rotation signal becomes narrower further downstream (See Fig. 4(d)). The changing of the thickness of the signal can be explained as the transition from the first stage of the acceleration, where the plasma bubble is expanding, to the second stage of the acceleration, where the plasma bubble becomes stable. The detail of the transition will be discussed in the next section.

Fig. 5(d) shows the electron spectrum for a shot in which accelerated electrons emerged in two bunches separated by $\sim 5 \text{ mrad}$ in a direction perpendicular to the spectrometer's energy dispersion plane. We observe such bifurcation occasionally when the drive laser focuses to a double-peaked intensity envelope, causing it to split into two filaments that drive parallel self-injected bubbles. The corresponding Faraday rotation signal (Fig. 5(b) shows broader structure in the bifurcation direction (y) than single-bubble shots (Fig. 3), indicative of the "doublebubble" structure of the interaction region.

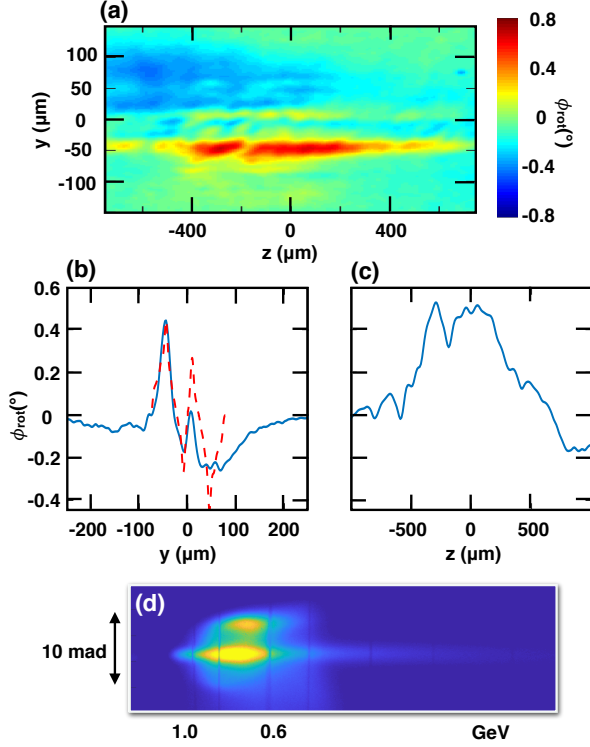


FIG. 5. (a) The spectrum that shows two electron bunches. (b) The Faraday rotation signal of the same shot. (c) The vertical lineout of the Faraday rotation signal averaged from $z = -400$ to $400 \mu\text{m}$. The red dash line is the result of FDTD simulation (see Fig. 9). (d) The horizontal lineout of the Faraday rotation signal averaged from $y = -80 \mu\text{m}$ to $-30 \mu\text{m}$. (d) The energy spectrum of the electron on the same shot. The total charge above 300 MeV is 132.3 pC.

IV. FDTD SIMULATIONS AND DISCUSSION

In order to reveal the connection between the plasma bubble structures and the Faraday rotation signals, we performed a series of finite difference time domain (FDTD) simulations. In the FDTD simulations, we sent a plane wave through static dielectric structures of the plasma bubble. The parameters of the dielectric structures were taken from a cylindrically symmetric PIC wakefield simulation^{2,14}. The PIC simulation was performed by using WAKE, a fully relativistic PIC code in axisymmetric geometry. (see Fig. 6)

Ideally, to obtain the Faraday rotation accurately, one needs to solve the eigenmodes and the dispersion relations of each grid and calculate the overall rotation (we call it ϕ_1) of the polarization of the probe beam after propagating through the magnetized plasma. However, solving eigenmodes and dispersion relation for each grid is time-consuming and not practical in simulations.

To simplify the problem, we considered only the $\mathbf{B}_\varphi \cdot \hat{\mathbf{k}}$ component of the magnetic field, where $\hat{\mathbf{k}}$ denotes the normalized wave vector of the probe beam (in our case,

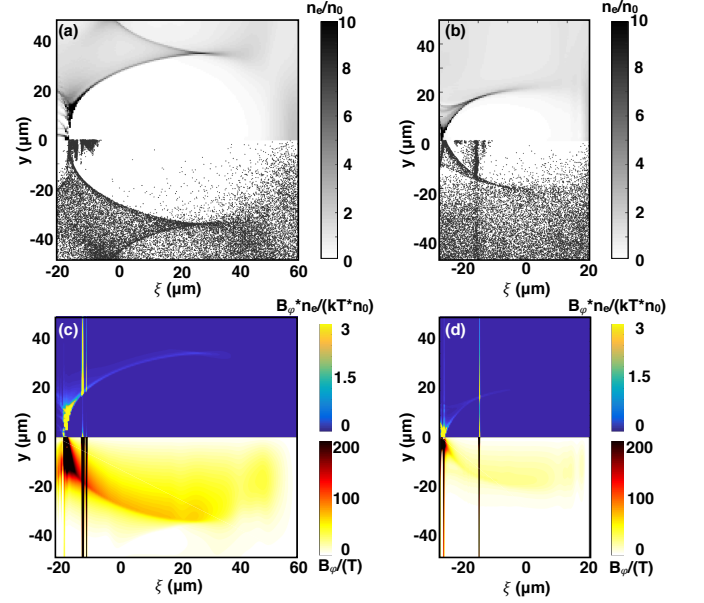


FIG. 6. Simulation data from a cylindrically symmetric PIC code, WAKE. (a) and (b) plasma density (upper half) ($n_0 = 4.8 \times 10^{17} \text{ cm}^{-3}$) and test particle distribution (lower half). The red dash lines are the contour lines of the driving pulse intensity. (c) and (d) $B_\varphi \cdot n_e$ (upper half) and B_φ (lower half) of the bubble. (a) and (c) Immediately after the self-injection happens. (b) and (d) 6 cm downstream after self-injection.

$\hat{\mathbf{k}} = \hat{\mathbf{x}}$), so the dielectric constant can be simplified as

$$\tilde{\epsilon}_r^\pm = 1 - \frac{\tilde{\omega}_p^2}{\tilde{\omega}(\tilde{\omega} \pm \tilde{\Omega}_B)}, \quad (2)$$

where $\tilde{\Omega}_B = e \cdot \tilde{B}_\varphi \cos(\theta) / m_e$ is the cyclotron frequency, θ is the angle between $\tilde{\mathbf{B}}_\varphi$ and $\hat{\mathbf{k}}$, $\tilde{\omega}_p = \sqrt{\frac{\tilde{n}_e e^2}{\epsilon_0 m_e}}$ is the plasma frequency, $\tilde{\omega}$ is the frequency of the probe beam, and \pm represents the right-handed and left-handed circularly polarized eigenmodes. The symbol \sim denotes that the quantities are in the plasma rest frame. The rotation angle can now be written as

$$d\tilde{\phi}_2 = \frac{\tilde{\omega}}{c} \left(\sqrt{1 - \frac{\tilde{\omega}_p^2}{\tilde{\omega}(\tilde{\omega} - \tilde{\Omega}_B)}} - \sqrt{1 - \frac{\tilde{\omega}_p^2}{\tilde{\omega}(\tilde{\omega} + \tilde{\Omega}_B)}} \right) dx \quad (3)$$

Here, dx represents an infinitesimal step of the probe beam.

Furthermore, when $\tilde{\Omega}_B \ll \tilde{\omega}$, Eq. (3) can be simplified as

$$d\tilde{\phi}_3 = \frac{\tilde{\omega}_p^2 \cdot \tilde{\Omega}_B}{2\tilde{\omega}^2 c} dx, \quad (4)$$

which ultimately leads to the expression of Eq. (1). The comparison of different methods of obtaining Faraday ro-

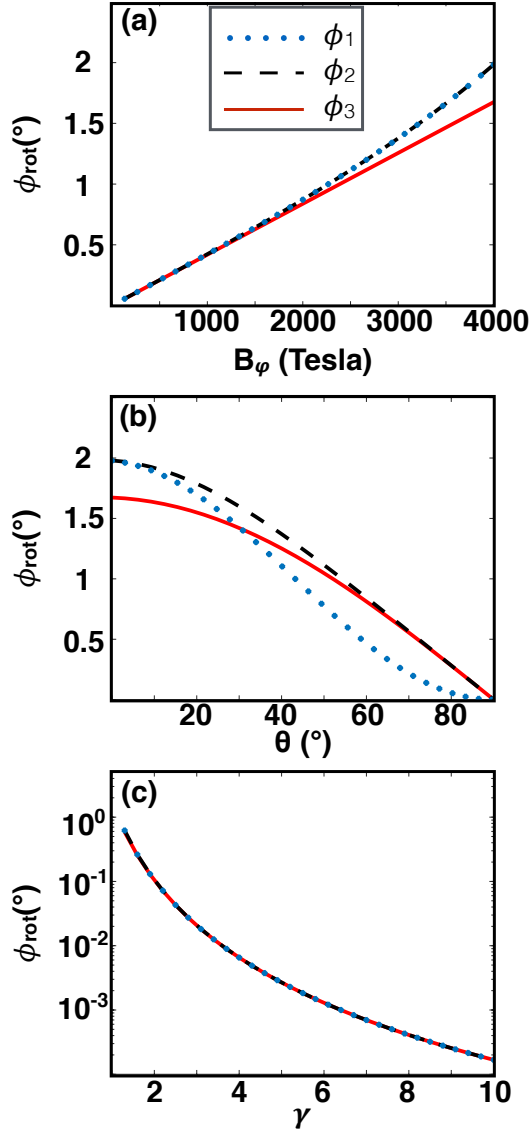


FIG. 7. Faraday rotation angle calculated by different approaches. ϕ_1 is the obtained by finding the eigenmodes and solving the dispersion relations. ϕ_2 is calculated by Eq. (3), and ϕ_3 is calculated by Eq. (4). (a) ϕ_{rot} versus the magnitude of the magnetic field. $\theta = 0^\circ$. The plasma thickness is $\Delta x = 50 \mu\text{m}$. (b) ϕ_{rot} versus the angle between \mathbf{B}_ϕ and $\hat{\mathbf{k}}$. $B_\phi = 4000$ Tesla. $\Delta x = 50 \mu\text{m}$. (c) ϕ_{rot} versus the Lorentz factor of the plasma flow. $\theta = 0^\circ$, and $B_\phi = 4000$ Tesla. $\Delta x = 50 \mu\text{m}$.

tation angle (ϕ_1 , ϕ_2 , and ϕ_3) is shown in Fig. 7. Although ϕ_2 is not exactly the analytical solution (ϕ_1), it is easier to calculate, and it slightly deviates from ϕ_1 only when θ is close to 90° where the rotation is already small. Therefore, in the following FDTD simulations, we will use Eq. (2) to calculate the dielectric constant. Since the data of the PIC simulation are in the lab frame, we are going to simplify the problem and ignore the difference between the plasma rest frame and the lab frame,

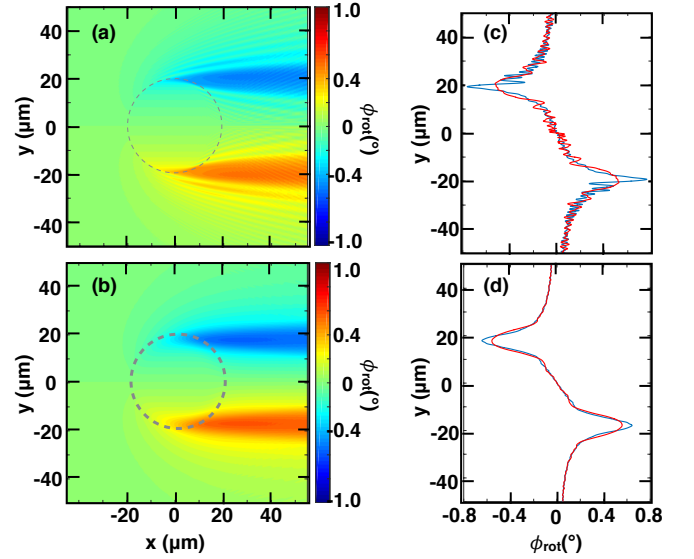


FIG. 8. (a) and (b) 2D FDTD Simulation of the Faraday rotation induced by the plasma bubbles. The thickness of the the bubble walls are 1.64 and 8.23 μm respectively. (c) and (d) Lineouts of the simulated rotation angle signals imaged by a near perfect imaging system ($f/0.08$). The object planes are on the center of the plasma bubble (in-focus, blue lines) and 30 μm downstream (out-of-focus, red lines).

and we will discuss the difference afterwards.

In the first step, we performed two 2D FDTD simulations. We took a slice of the plasma bubble at the location of the accelerated electron bunch from the PIC simulation ($\xi = \xi_0 = -17 \mu\text{m}$ in Fig. 6 (a) and (c)), calculated the dielectric distribution of the bubble slice, namely, $\epsilon_r^\pm(x, y, \xi = \xi_0) = 1 - \frac{\omega_p(x, y, \xi = \xi_0)^2}{\omega(\omega \pm \Omega_B(x, y, \xi = \xi_0))}$, and sent a plane wave through the dielectric structure. The plane wave propagated along x-axis and was linearly polarized in y-axis. The wavelength of the plane wave was 1.054 μm , the same as the probe beam in the experiment.

In order to reveal the connection between the Faraday rotation signal to the thickness of the bubble walls, we varied the thickness of the plasma density of the bubble wall while kept the total particle numbers conserved. The FWHM of the bubble wall densities were 1.64 and 8.23 μm , and the peaks of the densities were 7.4 and $1.48 \times 10^{18} \text{ cm}^{-3}$ respectively.

Fig. 8 shows the results of the 2D FDTD simulations. The plane wave propagates from left to right, and the polarization of the beam is along the y-axis. The color scale shows the polarization rotation of the probe beam (Fig. 8 (a) and (b)), and the lineout plots (Fig. 8 (c) and (d)) show the rotation angle signals imaged at the center of the bubble by a nearly perfect ($f/0.08$) imaging system.

In Fig. 8(c) and (d), we chose two different object planes, one at the center of the bubble (in-focus, blue line) and the other one 30 μm downstream (out-of-focus, red line). The out-of-focused rotation angle signal was

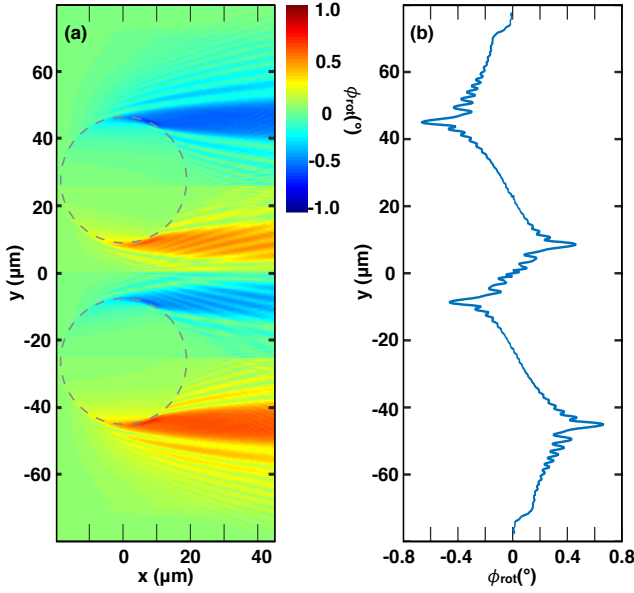


FIG. 9. 2D FDTD Faraday rotation simulation induced by two plasma bubbles. The parameters of the bubble walls is the same as Fig. 8(a), and the distance between the centers of the bubbles is $55 \mu\text{m}$. (a) The Faraday rotation angle (b) The rotation angle imaged at the center of the bubble by a near perfect imaging system ($f/0.08$).

diffracted (Fig. 8 (d) red lines) when the thickness of the bubble wall was close to the wavelength of the probe beam.

In both cases, the distance between peak and valley of the rotation angles matches the diameter of the plasma bubble, which proves that Faraday rotation occurs preferentially on the bubble walls. The theoretical estimation of the maximum value of the rotation angle was $\sim 1^\circ$, which agrees with the simulation results.

In addition, we perform a 2D FDTD Faraday rotation simulation with two bubbles, where the parameter of the bubble wall was the same as the thin wall case in the previous discussion (See Fig. 8(a)). The result is shown in Fig. 9. The distance between the center of the two bubbles is $55 \mu\text{m}$. Note that the magnitude of the rotation angle in the middle is smaller because the azimuthal magnetic field around the two bubbles cancel each other, which agrees with the experimental data (see Fig. 5(b)).

To interpret the experimental results further, we extended the 2D simulation and performed two 2D+1 FDTD simulations. This time, we calculated the dielectric distribution of the bubble as $\epsilon_r^\pm(x, y, \xi) = \sum_i \epsilon_r^\pm(x = x_i + \xi, y, \xi)$, and sent a plane wave along $x = \xi$ axis, which means that the plane wave overlapped with the bubble with 45° , as how the probe beam actually overlapped with the bubble in the experiment. Here, $\{x_i\}$ are the pixels on the x axis from the PIC simulation. Similar to the 2D simulation, the probe beam was linearly polarized in y-axis. The difference here is that, instead of using a thin plane wave, we added a pulse length to the probe

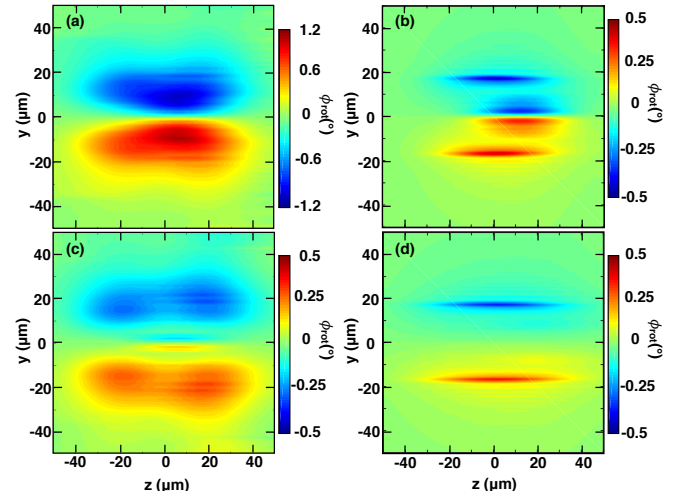


FIG. 10. Faraday rotation signals from 2D+1 FDTD simulation. (a) The rotation angle of the probe beam after propagating through the bubble in the first stage of the acceleration. (b) The rotation angle of the probe beam after propagating through the bubble in the second stage of the acceleration. (c) The rotation angle of the first stage after considering the relativistic effect. (d) The rotation angle of the second stage after considering the relativistic effect.

beam where $\tau_L = 100 \text{ fs}$.

We took two different bubble parameters from the PIC simulation. The first bubble parameter was immediately after the self-injection happened where the bubble was expanding (Fig. 6 (a)). This was in the first stage of the acceleration process. The other bubble structure was 6 cm downstream after self-injection happened where the bubble stabilized (Fig. 6(b)). This was the second stage of the acceleration process.

In the first stage of the acceleration when the bubble is expanding, large amounts of electrons, both passing electrons and injection candidates, aggregate on the back of the bubble ($n_e \sim 1 \times 10^{19} \text{ cm}^{-3}$). Moreover, about 98% of the electrons have forward momentum $P_z/(m_e c) > 10$ because they experience long slippage time around the bubble²⁴. Therefore, the electrons on the back of the bubble induce a strong azimuthal magnetic field ($> 500 \text{ T}$) (Fig. 6(c), bottom half). As a result, the injected electrons contribute little to $B_\varphi \cdot n_e$ (Fig. 6(c), top half) even though the magnetic field induced by them is $> 300 \text{ T}$ on the bubble wall. In the second stage of the acceleration, however, the electron aggregation on the back of the bubble reduces, and the azimuthal magnetic field is less intense on the back of the bubble (Fig. 6 (d), bottom half). Subsequently, the contribution of the accelerated electron bunch to $B_\varphi \cdot n_e$ is more significant (see Fig. 6(d), top half).

Fig. 10 shows the simulated Faraday rotation signals of the probe beam after propagating through the bubble. In the first stage of the acceleration (Fig. 10(a)), the vertical width of the signal is thick (FWHM $\sim 18 \mu\text{m}$), and the peak of the signal is close to the laser axis

due to the dense and thick plasma wall and strong magnetic field on the back of the bubble (see Fig. 6(c)). In the second stage, the vertical width of the peak becomes $\sim 4 \mu\text{m}$. The maximum of the rotation angle locates at $\sim 17.4 \mu\text{m}$ above the center (Fig. 10 (b)), while the intense region of $B_\phi \cdot n_e$ induced by the accelerated electron bunch is $16.58 \mu\text{m}$ above center (Fig. 6(d), upper half), which shows that the contribution of the electron bunch is more relevant in the second stage. Therefore, in the second stage, due of the reduction of $B_\phi \cdot n_e$ on the back of the bubble, the location of the maximum of the rotation angle can better represent the size of the bubble. However, the experimental results didn't show any significant peak close to the laser axis, while the simulation (Fig. 10 (a) and (b)) show strong signal near the center. The discrepancy of the experiment and simulation can be explained by considering the relativistic plasma flow of the bubble.

So far in the FDTD simulations, we assumed that the plasma bubble was static, and we used the data from the PIC simulation, which were in the lab frame, to calculate the dielectric constant ϵ_r . However, in reality, part of the plasma bubble (especially the back of the bubble) flew relativistically along with the driving beam. Therefore, we need to include the relativistic effect to calculate the dielectric constant in the plasma rest frame.

To calculate the dielectric constant in Eq. (2), we need to convert three quantities from the lab frame to the rest frame of plasma²⁶. The first one is the plasma density, $\tilde{n}_e = n_e/\gamma$. The second one is frequency of the probe beam, $\tilde{\omega} = \gamma(1 - \beta \cdot \hat{\mathbf{k}})\omega$, and the third one is the magnetic field, $\tilde{\mathbf{B}}_\phi = (\mathbf{1} + \gamma^2 \beta \beta) \cdot \mathbf{B}_\phi/\gamma$. Here γ is the Lorentz factor and β is the velocity of the plasma flow. After considering the relativistic effect of the plasma flow, the rotation angle ϕ_{rot} is proportional to $1/\gamma^4$ as shown in Fig. 7(c).

The result of FDTD simulation with the relativistic effect of the plasma flow is shown in Fig. 10(c) and (d). In Fig. 10(c), the magnitude of the rotation angle decreases drastically due to the relativistic effect. In particular, the rotation angle close to the laser axis is suppressed the most. Nevertheless, there is a residual peak at $y \simeq 2 \mu\text{m}$, and the vertical width of the rotation angle is still wide. On the other hand, the data in Fig. 10(d) shows almost no rotation in the region close to the laser axis, while the amount of the rotation away from the laser axis is nearly unchanged. The reason can be explained as follows.

Suppose that the bubble propagates through the plasma with velocity v_b (see Fig. 11). Electrons in the bubble wall flow around its periphery with velocity v_f in the bubble's rest frame. In a non-relativistic calculation for a "stable" bubble (Fig. 10(b)), streaming electrons at the side wall (position A on Fig. 11(a)) of the bubble contribute the outer Faraday shift lobe ($\sim 20 \mu\text{m}$ from axis), whereas streaming electrons at position B of Fig. 11(a) near the back of the bubble (5 to $10 \mu\text{m}$ from axis) contribute the inner lobe, which is not observed in

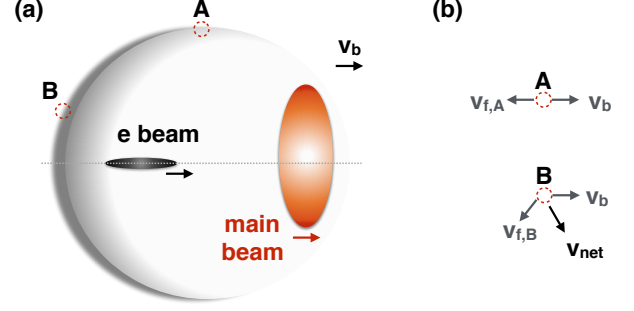


FIG. 11. Diagram of plasma bubble and the plasma flow. (a) plasma bubble induced by a laser pulse. (b) qualitative explanation of the plasma net flow at different positions of the bubble wall in the lab frame.

the experiments. In the lab frame (where the measurement is made), electrons at the side wall have velocity $v_b - v_{f,A} \sim 0$ (see Fig. 11(b)), whereas electrons at the back of the bubble have velocity $v_{net} \sim 0.97c$ ($\gamma \sim 4$) given by the vector sum of v_b and $v_{f,B}$. Consequently the Faraday rotation from these electrons is suppressed by a factor $1/\gamma^4 \sim 1/256$. This explains the relative weakness of the shift near the propagation axis.

By comparison, the Faraday rotation signal from the first stage (Fig. 10(c)) is similar to the data shown in Fig. 3(c) in terms of the wide vertical width and the small zero rotation region close to the laser axis. In the second stage (Fig. 10(d)), the narrow vertical width of the rotation angle signal and the bigger zero rotation region between the peak-and-valley are better resembled in the data in Fig. 4(c), which is 2 mm further downstream than Fig. 3(c). The difference between the two signals at different locations indicates that the bubble has fully blown out and started to proceed from the first stage to the second stage of the acceleration process in this region.

To summarize, the FDTD simulation showed that the Faraday rotation signals have different shapes and distributions when the bubble structures changes, especially in the two stages of acceleration. These simulation results indicated that, in the experiment, the plasma bubbles advanced from the first stage to the second stage at $\sim 61\%$ of the full laser-plasma interaction region. Furthermore, the relativistic effect of the plasma bubble flow can influence the magnitude and the shape of the rotation angle.

V. CONCLUSION

In conclusion, we were able to measure the transverse diameter of plasma bubbles of GeV LPAs using Faraday rotation diagnostics. The experimental results showed that the bubble advanced from the first stage to the second stage of the acceleration process at $\sim 61\%$ of full laser-plasma interaction region. The FDTD simulations

suggested that the Faraday rotation signals are sensitive to the plasma bubble structures.

ACKNOWLEDGMENTS

This work is sponsored by DOE and NSF by grant No. DE-SC0011617. Special thanks to all members in the Texas Pettawatt group and technical writer Harriett Hardman for editing the article.

- ¹T. Tajima and J. Dawson, "Laser electron accelerator," *Physics Review Letter* **43**, 267–270 (1979).
- ²X. Wang, R. Zgadzaj, N. Fazel, Z. Li, S. A. Yi, X. Zhang, W. Henderson, Y. Y. Chang, R. Korzekwa, H. E. Tsai, C. H. Pai, H. Quevedo, G. Dyer, E. Gaul, M. Martinez, A. C. Bernstein, T. Borger, M. Spinks, M. Donovan, V. Khudik, G. Shvets, T. Ditmire, and M. C. Downer, "Quasi-monoenergetic laser-plasma acceleration of electron to 2 gev," *Nature Communication* **4**, 1988 (2013).
- ³H. E. Tsai, X. Wang, J. M. Shaw, Z. Li, A. V. Arefiev, X. Zhang, R. Zgadzaj, W. Henderson, V. Khudik, G. Shvets, and M. C. Downer, "Compact tunable compton x-ray source from laser-plasma accelerator and plasma mirror," *Physics of Plasmas* **22**, 023106 (2015).
- ⁴K. Lotov, "Blowout regimes of plasma wakefield acceleration," *Physical Review E* **69**, 046405 (2004).
- ⁵A. Pukhov and J. Meyer-Ter-Vehn, "Laser wake field acceleration: the highly non-linear broken-wave regime," *Applied Physics B* **74**, 355–361 (2002).
- ⁶N. Barov, J. B. Rosenzweig, M. C. Thompson, and R. B. Yoker, "Energy loss of a high-charge bunched electron beam in plasma: Analysis," *Physical Review Special Topics - Accelerators and Beams* **7**, 60–70 (2004).
- ⁷I. Kostyukov, A. Pukhov, and S. Kiselev, "Phenomenological theory of laser-plasma interaction in "bubble" regime," *Physics of Plasmas* **11**, 5256 (2004).
- ⁸W. Lu, C. Huang, M. Tzoufras, F. S. Tsung, W. B. Mori, and T. Katsouleas, "A nonlinear theory for multidimensional relativistic plasma wave wakefields," *Physics of Plasmas* **13**, 056709 (2006).
- ⁹A. G. R. Thomas, "Scalings for radiation from plasma bubbles," *Physics of Plasmas* **17**, 056708 (2010).
- ¹⁰C. Benedetti, C. B. Schroeder, E. Esarey, F. Rossi, and W. P. Leemans, "Numerical investigation of electron self-injection in the nonlinear bubble regime," *Physics of Plasmas* **20**, 103108 (2013).
- ¹¹D. H. Froula, C. E. Clayton, T. Doppner, R. A. Fonseca, K. A. March, C. J. Barty, L. Divol, S. H. Glenzer, C. Joshi, W. Lu, S. F. Martins, P. Michel, W. Mori, J. P. Palastro, B. B. Pollock, A. Pak, J. E. Ralph, J. S. Ross, C. Sider, L. O. Silva, and T. Wang, "Measurements of the critical power for self-injection of electrons in a laser wakefield accelerator," *Physical Review Letters* **103**, 215006 (2009).
- ¹²S. P. D. Mangles, G. Genoud, M. S. Bloom, M. Burza, Z. Najmudin, A. Persson, K. Svensson, A. G. R. Thomas, and C.-G. Wahlstrom, "Self-injection threshold in self-guided laser wakefield accelerators," *Physical Review Special Topics - Accelerators and Beams* **15**, 011302 (2012).
- ¹³S. Kalmykov, S. A. Yi, V. Khudik, and G. Shvets, "Electron self-injection and trapping into an evolving plasma bubble," *Physical Review Letters* **103**, 135004 (2009).
- ¹⁴S. Y. Kalmykov, S. A. Reed, S. A. Yi, A. Beck, A. F. Lifschitz, X. Davonie, E. Lefebvre, V. Khudik, G. Shvets, P. Dong, X. Wang, D. Du, S. Bedacht, Y. Zhao, W. Henderson, A. Bernstein, G. Dyer, M. Martinez, E. Gaul, T. Dimire, and M. C. Downer, "Laser wakefield electron acceleration on texas petawatt facility: Towards multi-gev electron energy in a single self-guided stage," *High Energy Density Physics* **6**, 200–206 (2010).
- ¹⁵J. Faure, Y. Glinec, J. J. Santos, F. Ewald, J.-P. Rousseau, S. Kiselev, A. Pukhov, T. Hosokai, and V. Malka, "Observation of laser-plasma shortening in nonlinear plasma wave," *Physical Review Letters* **95**, 205003 (2005).
- ¹⁶W. Lu, M. Tzoufras, C. Joshi, F. S. Tsung, W. B. Mori, J. Vieira, R. A. Fonseca, and L. O. Silva, "Generating multi-gev electron bunches using single stage laser wakefield acceleration in a 3d nonlinear regime," *Physical Review Special Topics - Accelerators and Beams* **10**, 061301 (2007).
- ¹⁷P. Dong, S. A. Reed, S. A. Yi, S. Kalmykov, G. Shvets, and M. C. Downer, "Formation of optical bullets in laser-driven plasma bubble accelerators," *Physical Review Letters* **13**, 134801 (2010).
- ¹⁸Z. Li, H. E. Tsai, X. Zhang, C. H. Pai, Y. Y. Chang, R. Zgadzaj, X. Wang, V. Khudik, G. Shvets, and M. C. Downer, "Single-shot visualization of evolving laser wakefield using an all-optical streak camera," *Physical Review Letters* **113**, 085001 (2014).
- ¹⁹A. Savert, S. P. D. Mangles, M. Schnell, E. Siminos, J. M. Cole, M. Leier, M. Reuter, M. B. Schwab, M. Moller, K. Poder, O. Jackel, G. G. Paulus, C. Spielmann, S. Skupin, Z. Najmudin, and M. C. Kaluza, "Direct observation of the injection dynamics of a laser wakefield accelerator using few-femtosecond shadowgraphy," *Physical Review Letters* **115**, 055002 (2015).
- ²⁰Z. Li, "Single-shot visualization of evolving , light-speed refractive index structures," UT Austin Dissertation (2014).
- ²¹M. C. Kaluza, H.-P. Schlenvoigt, S. P. D. Mangles, A. G. R. Thomas, A. E. Dangor, H. Schwoeger, W. B. Mori, Z. Najmudin, and K. M. Krushelnick, "Measurement of magnetic-field structure in a laser-wakefield accelerator," *Physical Review Letters* **105**, 115002 (2010).
- ²²A. Flacco, J. Vieira, A. Lifschitz, F. Sylla, S. Kahaly, M. Veltcheva, L. O. Silva, and V. Malka, "Persistence of magnetic field driven by relativistic electrons in a plasma," *Nature Physics* **11**, 409–413 (2015).
- ²³A. Buck, M. Nicolai, K. Schmid, C. M. S. Sears, A. Savert, M. Mikhailova, F. Krausz, M. C. Kaluza, and L. Veisz, "Real-time observation of laser driven electron acceleration," *Nature Physics* **7**, 543–548 (2011).
- ²⁴S. Y. Kalmykov, A. Beck, S. A. Yi, V. N. Khudik, M. C. Downer, E. Lefebvre, B. A. Shadwick, and D. P. Umstadter, "Electron self-injection into an evolving plasma bubble: Quasi-monoenergetic laser-plasma acceleration in the blowout regime," *Physics of Plasmas* **18**, 056704 (2011).
- ²⁵S. A. Yi, V. Khudik, C. Siemon, and G. Shvets, "Analytic model of electromagnetic fields around a plasma bubble in the blow-out regime," *Physics of Plasmas* **20**, 013108 (2013).
- ²⁶A. E. Broderick and A. Loeb, "Signatures of relativistic helical motion in the rotation measures of active galactic nucleus jets," *The Astrophysical Journal* **703**, L104–L108 (2009).
- ²⁷I. Kostyukov, E. Nerush, A. Pukhov, and V. Seredov, "Electron self-injection in multidimensional relativistic-plasma wake fields," *Physical Review Letters* **103**, 175003 (2009).
- ²⁸W. Lu, C. Huang, M. Zhou, W. B. Mori, and T. Katsouleas, "Nonlinear theory for relativistic plasma wakefield in the blowout regime," *Physics Review Letter* **96**, 165002 (2006).
- ²⁹J. A. Stamper and B. H. Ripin, "Faraday-rotation measurements magnetic fields in laser-produced plasmas," *Physical Review Letters* **34**, 138 (1975).